ASPIRE Aerodynamic Models and Flight Performance

Suman Muppidi
AMA Inc., NASA Ames Research Center, Moffett Field, CA 94085, USA

Clara O'Farrell
Jet Propulsion Laboratory, California Institute of Technology, Pasadena, CA 91109, USA

John W Van Norman
AMA Inc., NASA Langley Research Center, Hampton, VA 23681, USA

and

Ian G Clark
Jet Propulsion Laboratory, California Institute of Technology, Pasadena, CA 91109, USA

The Advanced Supersonic Parachute Inflation Research Experiments (ASPIRE) project was launched to develop the capability for testing supersonic parachutes at Mars-relevant conditions. Three initial parachute tests, targeted as a risk-reduction activity for NASA's upcoming Mars2020 mission, successfully tested two candidate parachute designs and provided valuable data on parachute inflation, forces, and aerodynamic behavior. Design of the flight tests depended on flight mechanics simulations which in turn required aerodynamic models for the payload, and the parachute. Computational Fluid Dynamics (CFD) was used to generate these models pre-flight and are compared against the flight data after the tests. For the payload, the reconstructed aerodynamic behavior is close to the pre-flight predictions, but the uncertainties in the reconstructed data are high due to the low dynamic pressures and accelerations during the flight period of comparison. For the parachute, the predicted time to inflation agrees well with the pre-flight model; the peak aerodynamic force and the steady state drag on the parachute are within the bounds of the pre-flight models, even as the models over-predict the parachute drag at supersonic Mach numbers. Notably, the flight data does not show the transonic drag decrease predicted by the pre-flight model. The ASPIRE flight tests provide previously unavailable valuable data on the performance of a large full-scale parachute behind a slender leading body at Mars-relevant Mach number, dynamic pressure and parachute loads. This data is used to propose a new model for the parachute drag behind slender bodies to aid future experiments.

I. Introduction

Disk-Gap-Band (DGB) parachutes have been used by every American entry mission to Mars, from the Viking twin landers in 1975 [1] to the InSight lander in 2018, to decelerate from low supersonic speeds to the low subsonic speeds required for terminal descent. The DGB parachute was designed, developed, and tested during series of development campaigns undertaken by NASA in the 1960's and 1970's that included wind tunnel tests [2-4], low altitude drop tests [5], and high-altitude supersonic parachute test programs [6-8]. This developmental activity resulted in the qualification of the 16.2-m parachute behind a representative capsule in low-density conditions via a Balloon-Launched-Decelerator-Test (BLDT) [9] series, and the successful landing of Viking 1 and Viking 2 in July and September of 1976. Subsequent NASA missions to Mars (Mars Pathfinder [10], [11], Mars Polar Lander [12], Mars Exploration Rovers [13], Phoenix Lander [14], Mars Science Laboratory [15], and the InSight Lander[16]) modified the Viking parachute design and responded to advances in parachute technology (utilization of new materials, for example) and the different mission requirements. While these missions conducted subscale developmental tests and/or subsonic full-scale testing, none of these parachutes were qualified supersonically at full scale prior to deployment at Mars.

The *Advanced Supersonic Parachute Inflation Research Experiments* (ASPIRE) project was launched in 2016 to develop a capability for testing supersonic parachutes at Mars-relevant conditions. The initial series of ASPIRE flights were focused on testing two candidate parachutes at Mach and dynamic pressure relevant to the Mars2020 project: a build-to-print version of the parachute used by the Mars Science Laboratory (MSL) in 2012 and a full-scale strengthened version of this parachute that has the same geometry but differs in materials and construction. Tanner et al. [17] provide details of the two parachutes, a summary of their differences, and an overview of the Mars2020 parachute program's risk reduction efforts. The ASPIRE parachutes were delivered to targeted deployment conditions at high altitudes over Earth by NASA's Sounding Rocket Operations Contract (NSROC) sounding rockets. The concept of operations for the ASPIRE sounding rocket tests is outlined in Figure 1. The sounding rocket assembly, consisting of a Terrier first stage, a Black Brant second stage, and the payload section containing the experiment, were launched from NASA's Wallops Flight Facility in Virginia. The system was rail-launched and spin-stabilized at 4 Hz during ascent. The first stage burned out soon after launch (approximately 700 m to 1000 m altitude) followed by a second stage ignition which itself burned out at an altitude of approximately 15.0 -16.0 km; the payload section reached apogee between 48 km and 55 km. During descent, when the payload reached the target dynamic pressure and Mach number conditions, the parachute was mortar-deployed from the back of the payload. The deployment, inflation, and supersonic and subsonic aerodynamics of the parachute were recorded by a suite of instruments including a three-camera high-speed/high-resolution stereographic video system trained on the parachute, situational awareness video cameras, load pins at the interface of the parachute triple-bridle and the payload, and a GPS and inertial measurement unit (IMU) onboard the payload. After decelerating to subsonic speed, the parachute and payload descended to the ocean roughly 30 min after launch.

Three flight tests were conducted as part of ASPIRE. The first sounding rocket flight test (designated as SR01) took place on October 4, 2017 [18], with the twin objectives of conducting a shake-out of the sounding rocket test architecture, and of deploying Mars2020's build-to-print parachute in a low-density supersonic test environment. During the second (SR02) and third (SR03) tests [19], which took place on March 31st and September 7th, 2018, the strengthened parachute was tested to incrementally higher parachute loads. All three flight tests were successful. The experiment was delivered to the desired test conditions by the launch vehicle, the test article was deployed successfully, the parachute and payload were recovered from the ocean, and the test data (parachute deployment imagery, parachute performance data) were collected and analyzed. Figure 1 shows timing and trajectory information of significant events during the first flight test. Key events for all the three flights are shown in Table 1. Also shown in Figure 1, in red, are the pre-flight (SR01) expectations for these parameters. For example, the pre-flight range for payload apogee was 42.4 to 60.2 km; the apogee achieved during the flight test was 51.0 km.

As part of designing the flight test, the Program to Optimize Simulated Trajectories II (POST2) [20] and Dynamics and Spacecraft Simulator for Entry, Descent and Surface Landing (DSENDS) [21] codes were used to simulate the test flights : starting from separation of the payload from Brant-stage, through parachute deployment and inflation, to the eventual splashdown. The simulations were used to help vehicle development,to conduct trade studies, to evaluate the vehicle trajectory (for targeting, range safety, parachute recovery), and to provide pre-flight predictions as shown in Figure 1 [22]. The simulations depend on models for payload aerodynamics and parachute performance including models for peak inflation load and for the parachute drag.

This paper describes the various aerodynamic models for the payload and parachute performance used in the pre-flight simulations. In addition to data from previous flight tests and experiments, where appropriate, the aerodynamic models were also influenced by computational fluid dynamics (CFD) simulations. The paper is organized as follows: Section II provides information on the Flight Test Architecture , section III provides an overview of the three flight tests, section IV describes the development and incorporation of the aerodynamics models for the payload including comparison of pre-flight predictions to the flight test data. Finally, section V presents the various models that were part of the parachute aerodynamics, followed by a brief summary.

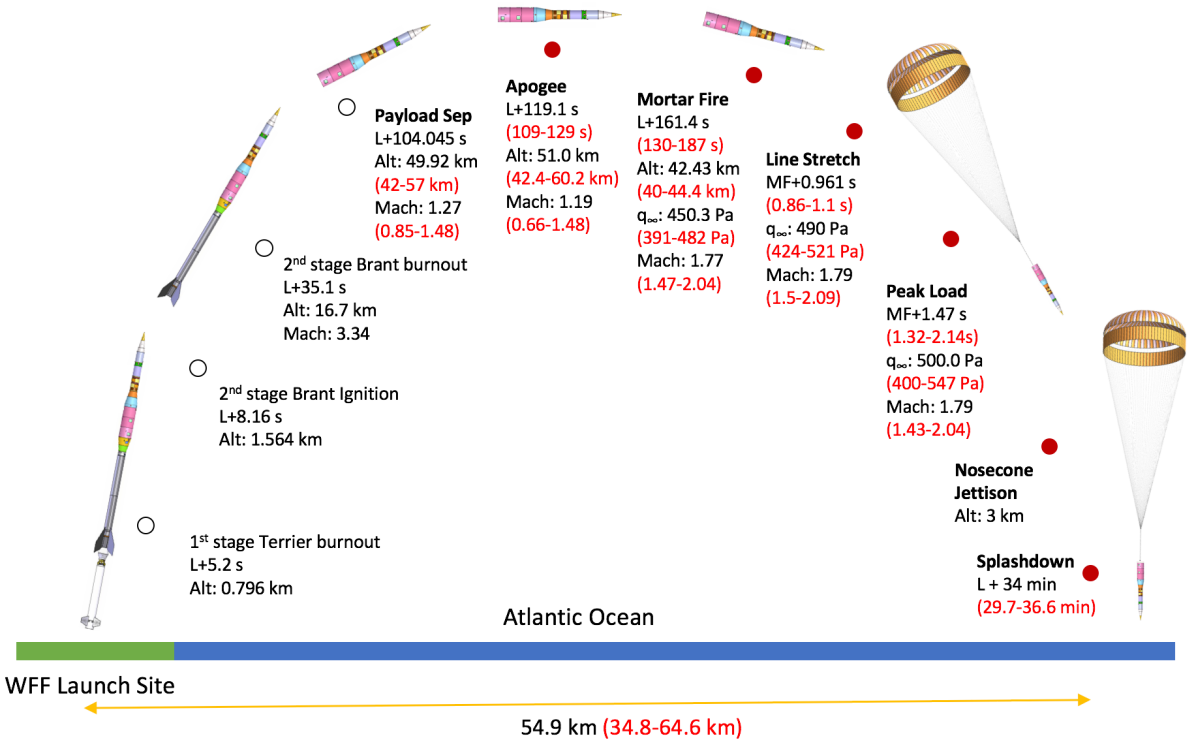

Figure 1 Schematic of the Flight test shows launch, delivery of the payload, parachute deployment and splashdown. The parameters in red show the expected range pre-flight, and the corresponding black text show the actual values during the first flight test SR01 (4th October 2017).

II. Test Architecture

Figure 2 shows the ASPIRE configuration prior to launch, and the ASPIRE payload after separation from the second stage motor (and prior to parachute deployment). The payload is, in essence, a large ballistic dart that carries the experimental hardware and the instrumentation [19]. The nose is heavily ballasted to minimize both deceleration during parachute inflation, and drift during the long descent; the ballast is jettisioned at about 3km altitude prior to splashdown to facilitate retrieval of the payload, the parachute, and the flight test data. The middle section of the payload contains flight electronics along with a cold gas Attitude Control System (ACS). The Experiment section towards the aft of the payload contains the packed parachute, deployment mechanism, and ASPIRE instrumentation including the multiple cameras. Figure 3 depicts the ASPIRE configuration after parachute deployment. While the diameter of the ASPIRE payload (parachute forebody) is 0.72 m, the reference diameter of the parchute is about 21.5m and its inflated diameter is roughly 15.6m. The leading edge of the parachute trails behind the nose of the payload by about 45m. Design values of L_S, L_R and L_B are 36.47m, 7.78m and 1.30 m respectively. The as-built dimensions of the parachutes are detailed in [18] and [19].

The instrumentation on the payload provides data on the trajectory and aerodynamic performance of both the payload and the parachute. The onboard instrumentation suite included an IMU, GPS, three load pins at the triple bridle, three high-speed cameras, and three situational video cameras. In addition, three ground-based radars were used to track the payload during flight; meteorological balloons carrying radiosondes that were released hourly during launch operations enable atmospheric reconstruction. Details of the instrumentation along with relevant data are provided in [18], [19] and [23].

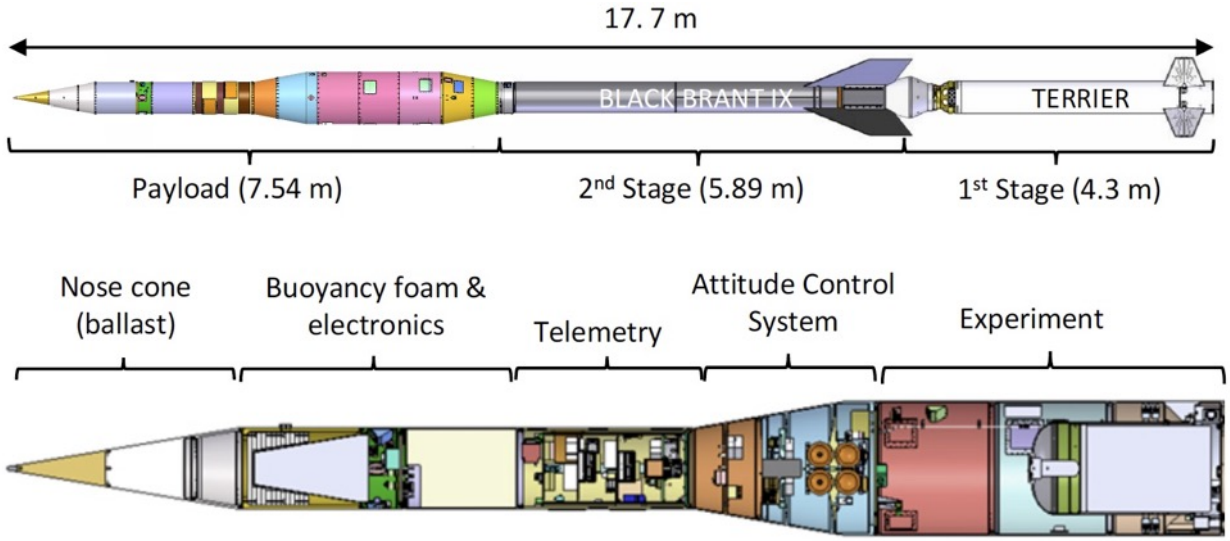

Figure 2 Schematic of the ASPIRE launch configuration and payload. Image on the top shows the configuration during launch, and image on the bottom shows the payload after separation from the second stage (and prior to parachute deployment).

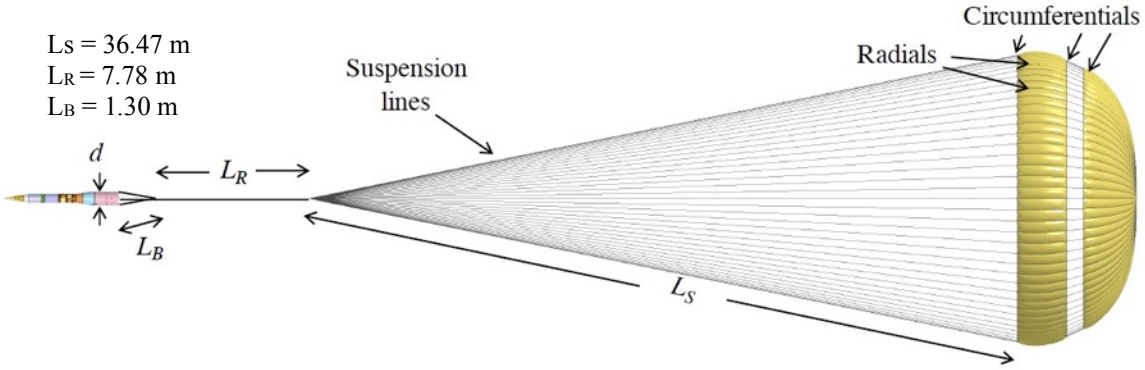

Figure 3 Schematic of the ASPIRE parachute system.

III. Flight Tests Overview

Table 1 presents relevant trajectory and performance information from all three flight tests (refer to [18] and [19] for more details). The times indicated are relative to launch. During the first flight test, the test vehicle began spinning (for gyroscopic stability) about 1.18 seconds after launch, and the 1st stage rocket burnt out about 6.23 seconds after launch, soon after which it separated and fell into the ocean. The second stage motor ignited soon after, accelerating the vehicle through supersonic speeds before burning out about 34 seconds after launch. Thereafter, the second stage motor and the payload traveled together, still spinning. At about 100 seconds after launch, de-spin motors fired to stop the vehicle from spinning, followed quickly by a payload separation. At this point, the payload was at Mach 1.27, an altitude of 49.92 km, and a fairly low dynamic pressure of 87.15 Pa, due to low air density. The payload reached an apogee of 51.0 km about 119 seconds after launch after which the payload began accelerating towards the earth. At 159.88 seconds after launch, the on-board computer recognized the pre-set target conditions and initiated the parachute deployment. The mortar was fired soon after, ejecting the packed parachute pack which sailed away from the payload, unraveling the suspension lines. Line stretch, the instant when parachute the rigging becomes taut and the canopy begins to inflate, occurred at 162.37 sec. Peak parachute load occured roughly 0.5 seconds later, at Mach 1.77 and a dynamic pressure of 494.88 Pa. This corresponds to full inflation. The parachute-payload system began decelerating soon after this, slowing down as they descended. The parachute and the payload finally splashed down into the Atlantic ocean almost half an hour later.

Table 1 Trajectory and Timing information from the three flight tests

		SR01	SR02	SR03
Date		October 4th 2017	March 31st 2018	September 7th 2018
Launch	Time (s)	0	0	0
Spin-up	Time (s)	1.18	1.19	1.11
1st Stage Burnout	Time (s)	6.23	6.21	5.54
Mach 1.0	Time (s)	11.98	11.69	12.21
Mach 2.0	Time (s)	12.16	22.84	23.64
Mach 3.0	Time (s)	30.04	30.31	30.69
2nd Stage Burnout	Time (s)	34.27	34.10	33.72
Despin	Time (s)	100.09	100.03	100.15
Payload Separation	Time (s)	104.03	103.99	104.06
	Mach	1.27	1.24	1.17
	dyn. Pressure (Pa)	87.15	53.80	96.41
Apogee	Time (s)	119.04	123.49	116.52
	altitude	51	54.82	48.85
Trigger	Time (s)	159.88	176.01	162.24
	Mach	1.73	1.92	1.81
Mortar Fire	Time(s)	161.41	177.58	163.81
	Mach	1.77	1.97	1.85
Line Stretch	Time (s)	162.37	178.62	164.85
Peak Load	Time (s)	162.88	179.08	165.25
	Mach	1.77	1.97	1.85
	dyn. Pressure (Pa)	494.88	746.5	1020.12
Splashdown	Time (s)	2056	2029.56	1982.21

All three flight tests underwent the same sequence of operations, with differences in the actual trajectory parameters: SR02 saw the highest altitude with an apogee of 54.82 km; and the highest Mach number at full inflation, of 1.97. The corresponding values for SR03 were 48.8 km and mach 1.85 respectively. Note that the three flight tests were designed to achieve incrementally higher parachute loads, by targeting increasing dynamic pressures at peak load. As shown in Table 1, the dynamic pressure at full inflation was 494.88 Pa for SR01, 746.5 Pa for SR02 and 1020.12 Pa for SR03.

IV. ASPIRE Payload Aerodynamics Model

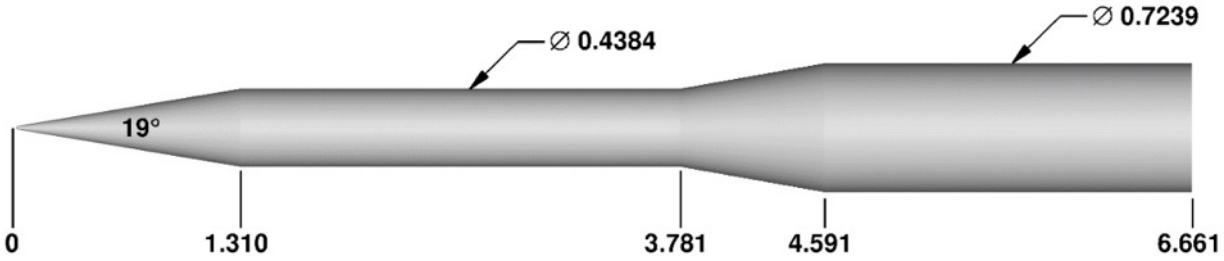

Figure 4 ASPIRE payload geometry with dimensions in meters.

The ASPIRE payload section (Figure 2) carried the experiment (including the packed parachute and instrumentation) and is designed to provide sufficient ballast to satisfy the infinite mass assumption for parachute inflation and deceleration. As shown in Figure 4, the basic configuration consisted of a conical nose cone with 9.5° half angle and 0.4384 m base diameter, followed by a cylindrical section, a conical transition to 0.7239 m diameter, and a second cylindrical section with a flat base. The overall length of the payload (after separation) was 6.6606 m. The mass of the payload was approximately 1100 kg (the exact mass varied from test-to-test depending on the parachute and the targeted trajectory).

The ASPIRE payload aerodynamic model was constructed for use by the flight dynamics team in targeting flight conditions and predicting the flight performance, and is comprised of tabulated aerodynamic coefficients and aerodynamic uncertainties. The model is invoked to calculate static aerodynamic coefficients for a given set of input arguments (instantaneous center of gravity (*cg*) location, freestream Mach number, angles of attack and sideslip, and uncertainty dispersions). At each time step of the flight simulation, the software passes the required arguments to the aerodynamic model which interpolates coefficients from the appropriate table, applies uncertainties, and returns static aerodynamic coefficients.

Table 2 Freestream conditions for CFD analysis, used to develop the ASPIRE payload database/model.

Altitude (km)	Temperature(K)	Density (kg/m3)	Mach Number	Velocity (m/s)	Dynamic Pressure (Pa)	Reynolds Numnber (1/m)
57.85	254.9	4.3e-4	0.9	288.0	18.0	7.7e3
55.61	264.0	5.6e-4	1.1	358.2	35.8	1.2e4
49.45	271.0	1.2e-3	1.5	495.0	150.4	3.6e4
39.27	258.6	4.9e-3	2.44	787.9	1521.1	2.3e5

ASPIRE payload aerodynamics were predicted using NASA-developed Computational Fluid Dynamic (CFD) codes, where the OVERFLOW[24] solver was used for production runs, and the FUN3D[25] and DPLR[26] codes were used for code-to-code comparisons and point checks over a subset of the simulation matrix. The aerodynamic model consists of static aerodynamic coefficients only. No pitch damping model was implemented, as none was deemed appropriate for ASPIRE's natural pitch cycle rate at nominal flight conditions (<< 1 Hz). The CFD simulations spanned a Mach number range of 0.9 to 2.45, and at total angles of attack α_T = 0, 2, 5, 10, 15, 20, 30, 45, 60, and 75°. The nominal aerodynamics and uncertainty models apply up to α_T = 30°; the remaining solution space is to cover possible off-nominal flight scenarios. Table 2 provides a list of freestream conditions used to generate the CFD solutions and the aerodynamics database, including the unit Reynolds number. A notable feature of the ASPIRE trajectories is the relatively low Reynolds numbers. At the lowest Mach number, for example, the Reynolds number associated with the payload length is lower than that associated with smooth wall turbulent transition, suggesting that portions of the boundary layer should remain laminar. There is a large uncertainty associated with transition prediction on relevant geometries at these Reynolds numbers. As a result, CFD simulations for the database included both laminar and turbulent flow solutions to help understand the sensitivity of payload aerodynamics to turbulence, and to viscous modeling.

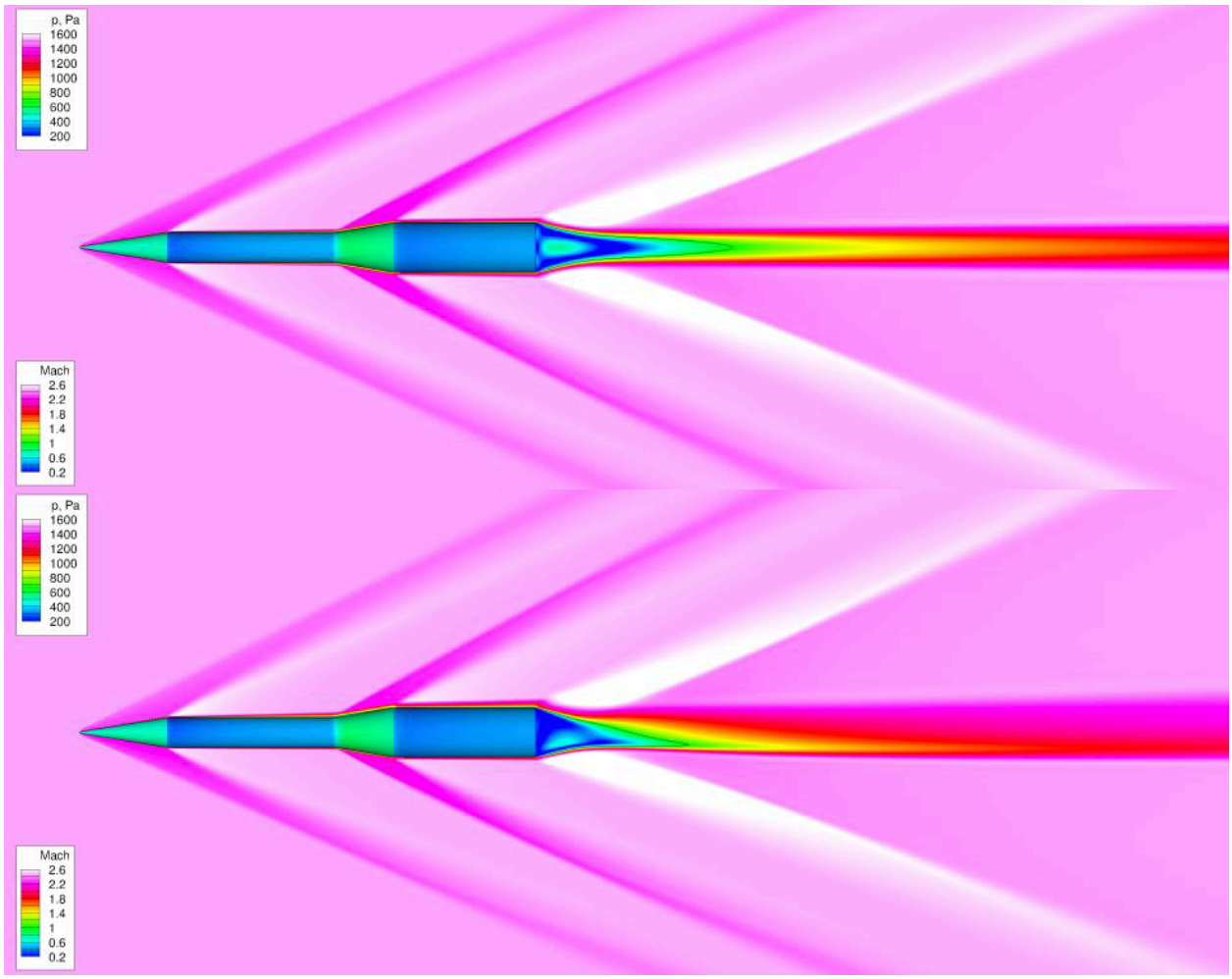

Figure 5 Surface pressure contours and symmetry plane Mach Number visualization from simulations at Mach 2.45. Angle of attack 0 deg (top) and 2 deg (bottom).

Figure 5 shows the flowfield from one of the simulations using contours of pressure on the surface of the payload, and Mach number on the symmetry plane. The freestream Mach number is 2.45, and the angles of attack are 0° and 2° on the top and bottom planels, respectively. The flow features a leading shock originating near the nose of the payload, an expansion at the first cone-cylinder junction, followed by a second conical shock and expansion as the payload diameter increases. Images also show the wake of the payload and the final expansion at the aft end.

As is typical of slender bodies, the ASPIRE payload aerodynamics are sensitive to viscosity; for example, at low angles of attack, the viscous contribution to drag exceeeded 20%. As a result, laminar and turbulent simulations yield different values for the aerodynamic coefficients. To develop the payload aerodynamic model, coefficients were averaged between laminar and turbulent solutions to yield the nominal coefficient, and uncertainties were chosen to cover the differences between laminar and turbulent solutions while leaving additional margin for unknowns. Figure 6 shows this approach using the axial force coefficient C_A at freestream Mach number 1.1. At various angles of attack, the symbols show both laminar and turbulent flow results – note that the differences decrease with increasing Mach number. The nominal C_A curve (shown as the solid black line) is obtained by averaging and interpolating. C_A increases with the angle of attack between 0° and 20°, shows a slight decrease between 20° and 25°. The figure also shows the 3-sigma uncertainty bounds (as dashed lines).

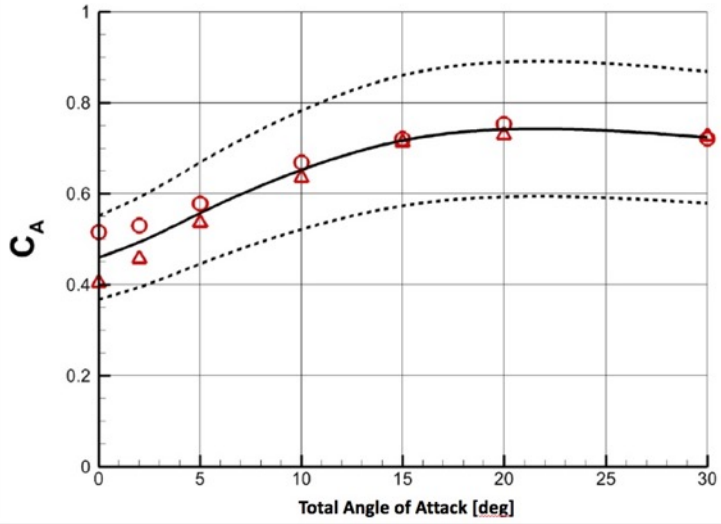

Figure 6 Variation of the axial force coefficient with angle of attack at Mach number 1.1.
circles: turbulent flow, triangles: laminar flow, solid line: nominal curve, dashed lines: uncertainty bounds

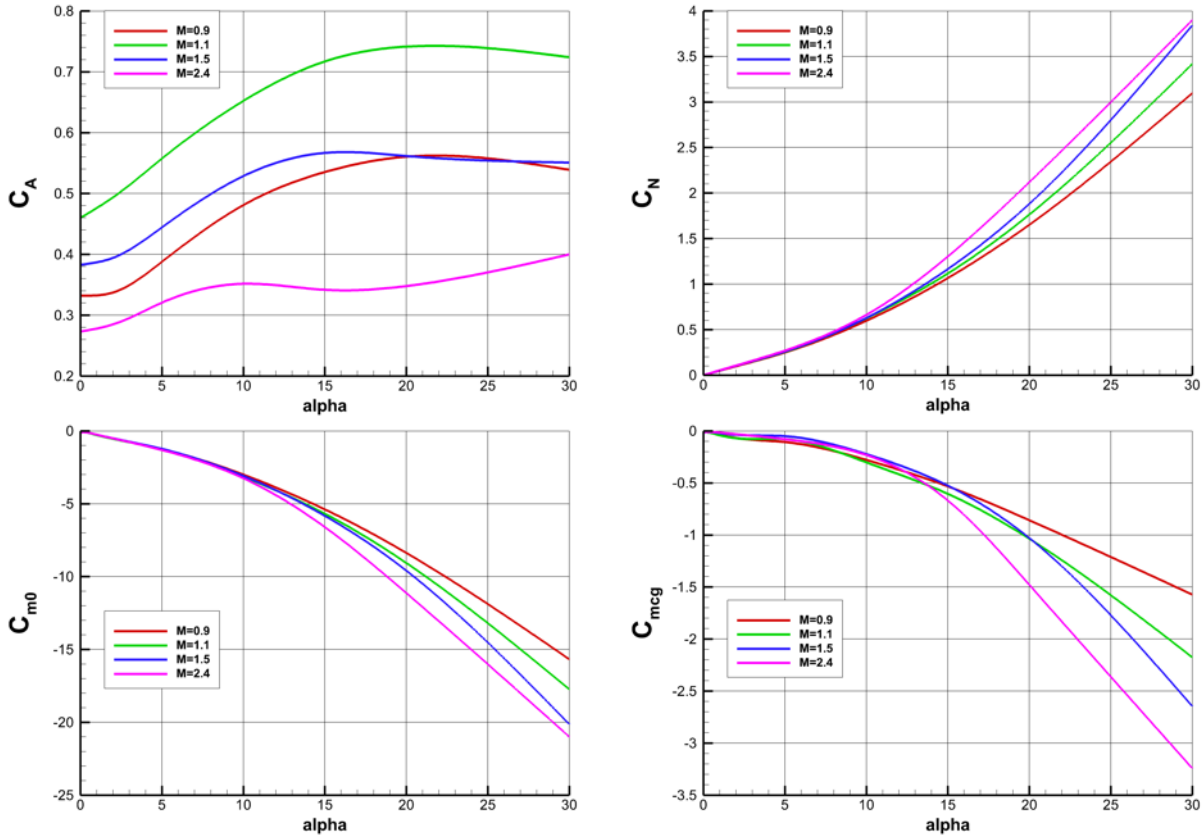

Figure 7 Variation of the payload aerodynamic coefficients with Mach number and angle of attack. Curves indicate the nominal model.

Figure 7 shows the nominal curves for axial and normal force coefficients, and pitching moment coefficient about both the nose and the payload center of gravity. With increasing Mach number, the axial force shows a non-monotonic behavior across the transonic range: it increases between Mach 0.9 and 1.1, and decreases threafter. The normal force coefficient appears to be almost independent of Mach number between roughly 0° and 10°, and is monotonic thereafter (with respect to both angle of attach and Mach number). The CFD simulations are used to compute the pitching

moment coefficient about the nose (C_{m0}) which is then transferred to yield the coefficient about the center of gravity (C_{mcg}). Like C_N, C_{m0} shows a behavior independent of Mach number at lower angles of attack and a monotonic variation after 15°. However, C_{mcg} exhibits a more complex variation: it is not strictly monotonic (with M) until 25° angle of attack; between 0° and 15°, the curves are close to each other.

As part of the flight mechanics simulations, dispersed aerodynamic coefficients are computed from the nominal coefficients/models (shown above) and the 3-sigma uncertainties as $C_{disp} = (C_{nom}+u_1 \times \text{adder})(1+u_2 \times \text{multiplier})$, where u_1 and u_2 are independent perturbations that vary between -1 and 1. These parameters are randomly generated at the beginning of the simulation and held constant through the duration of the flight. For a series of flight mechanics simulations as used for a Monte Carlo analysis, a new set of dispersion coefficients are generated for each run. The magnitude of the adders and the multipliers are informed by the CFD simulations, and the values used for various aerodynamic coefficients and are shown in Table 3. Moment coefficient dispersions are applied at the center of gravity (to make them independent of the moment transfer calculations). Uncertainty adders for the various coefficients are uncorrelated. However, multipliers for side and normal force uncertainties are; as are multipliers for pitch and yaw moment coefficient uncertainties.

Table 3 ASPIRE Payload uncertainties used to compute dispersed payload aerodynamic coefficients

Coefficient	Adder	Multiplier
C_A	0.0	0.2
C_N, C_Y	0.02	0.05
C_m, C_n	0.08	0.1

Post-Flight Reconstruction: Post-flight trajectory was reconstructed by the NewSTEP tool [27,28] using an atmospheric model, and data from on-board IMU, GPS and ground-based tracking radars. The reconstructed trajectory includes linear and angular accelerations, which in turn, are used to yield the static payload aerodynamics. The comparison to pre-flight predictions is limited to the descending part of the trajectory (from apogee to trigger) where the Mach number variation is monotonic in time. During this time, the cold-gas Attitude Control System (ACS) is active. Thrusters were periodically fired to null out residual roll rates and to keep payload angle of attack and sideslip near zero degrees. In order to isolate aerodynamic accelerations from the ACS firings, trajectory information during the firings (from the 'on' command to 0.1 second after the 'off' command) is removed from the analysis. Finally, raw accelerations provided by the IMU are filtered using a Laplacian operator to reduce the noise.

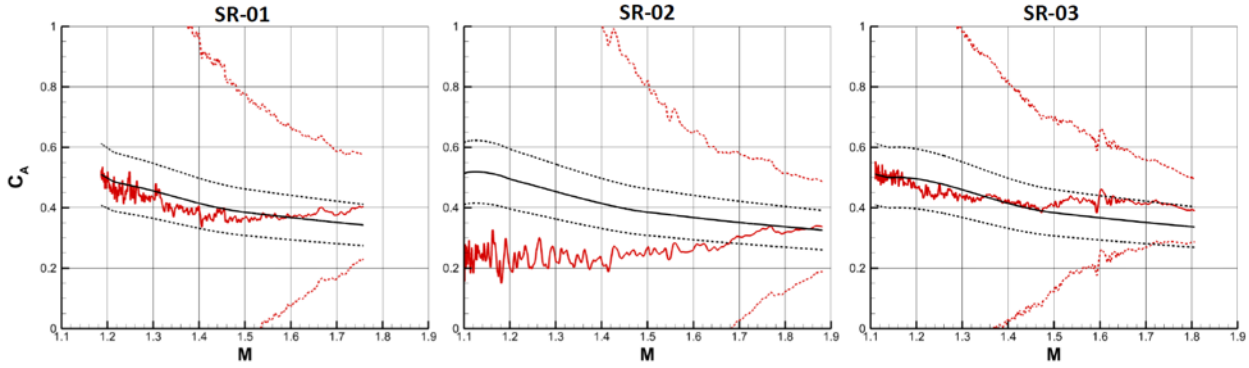

Figure 8 Reconstructed axial force coefficients compared to pre-flight predictions, from the three flights.Red: reconstructed data, black: Pre-flight database, dashed lines: uncertainties. Only the flight data between apogee and parachute deployment is shown

Figure 8 shows the reconstructed axial force coefficient as a function of the Mach number from the three flights, compared against pre-flight predictions and uncertainties for both. The curves show significantly high uncertainty in reconstructed aerodynamics, which is mostly attributable to the uncertainties in the IMU. Note that the accelerations being measured immediately after apogee were on the order of the resolution of the IMU, leading to this large uncertainty in reconstructing the payload aerodynamics. This is further exacerbated during SR02 owing to a higher altitude at apogee, a lower dynamic pressure and lower aerodynamic forces and resulting accelerations.

Reconstructed C_A (Figure 8) for the SR01 and SR03 flights appear to fall within the pre-flight bounds, even as it reaches the upper bound towards the end of the analysis period (highest Mach number). This is in contrast to data from SR02 test where C_A at the lower Mach numbers is significantly lower than the pre-flight predictions, and is out of family with SR01 and SR03 for most of the trajectory, even as it reaches the nominal curve towards the end (approximately near Mach 1.8). It is likely that the reconstructed SR01 and SR03 curves exhibit boundary layer

transition. A comparison of relative slopes between reconstructed and pre-flight predicted drag curves indicate a transition (from partially turbulent, to fully turbulent) at similar conditions: the slope changes around Mach 1.46 and at unit Reynolds number of 4.3e4 and 6.7e4 for SR01 and SR03 respectively. While these values are suggestive, they should not be considered conclusive: reconstructed data includes large uncertainties, and the assumption of perfect wind and atmospheric knowledge is unreasonable. For the sake of completeness, Figure 9 plots reconstructed coefficients for the normal force and moment from SR03 along with pre-flight predictions. However, the uncertainty in reconstruction is an order of magnitude higher than the value of the coefficient for C_N, and two orders of magnitude higher than the magnitude of $C_{m,cg}$.

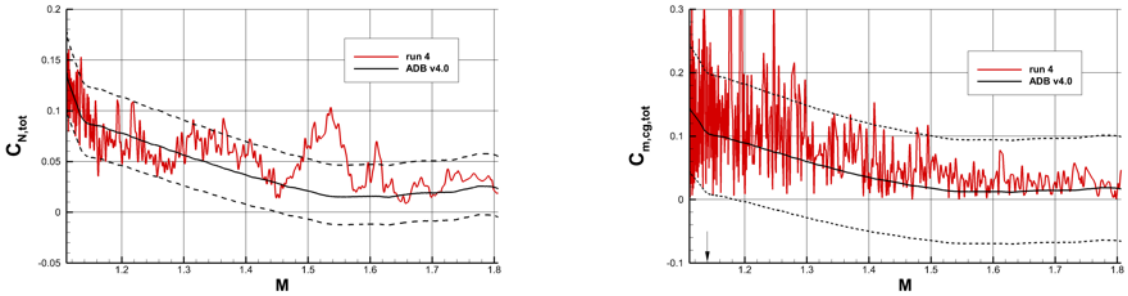

Figure 9 Reconstructed Normal Force Coefficient and Moment Coefficient from SR03 plotted against pre-flight prediction. Red: reconstructed data, black: Pre-flight database, dashed lines: uncertainties. Data from apogee to parachute deployment.

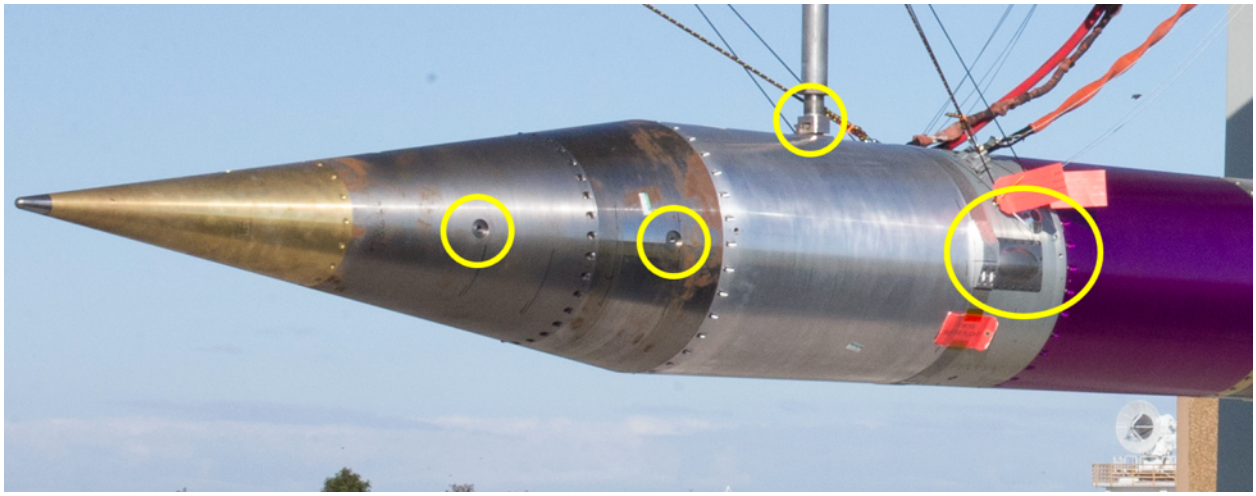

Figure 10 Image of the leading vehicle nose highlighting the multiple protuberances and cavities that could trip the boundary layer.

Pre-flight analysis assumed a smooth payload geometry, and both laminar and turbulent simulations were used to conservatively cover possibilities. However, the flight article features many protuberances and cavities, as shown in Figure 10, that could likely trip the flow and cause boundary layer transition even at the lower Reynolds numbers - even if the transition is only local. Consequently, it is not reasonable to expect the reconstructed coefficients to agree with the laminar flow predictions, or the lower bounds of the payload aerodynamic model. However, the comparisons validate the pre-flight aerodynamics models and the methodology. Even as the measurement uncertainties are high, the nominal curves agree well in most cases, and the trends (with increasing Mach number and Reynolds number) are reasonable.

V. ASPIRE Parachute Aerodynamic Models

As part of the flight test design, models were developed for all aspects of parachute performance, including deployment, inflation, opening loads, and aerodynamic drag. These models played a key role in predicting the peak load and accelerations during flight for structural analyses, selecting target test conditions, setting trigger values,

sensor selection and placement, evaluating range safety, and designing recovery operations. In this section, we describe the parachute aerodynamic models used in ASPIRE and compare the predictions against reconstructed flight results.

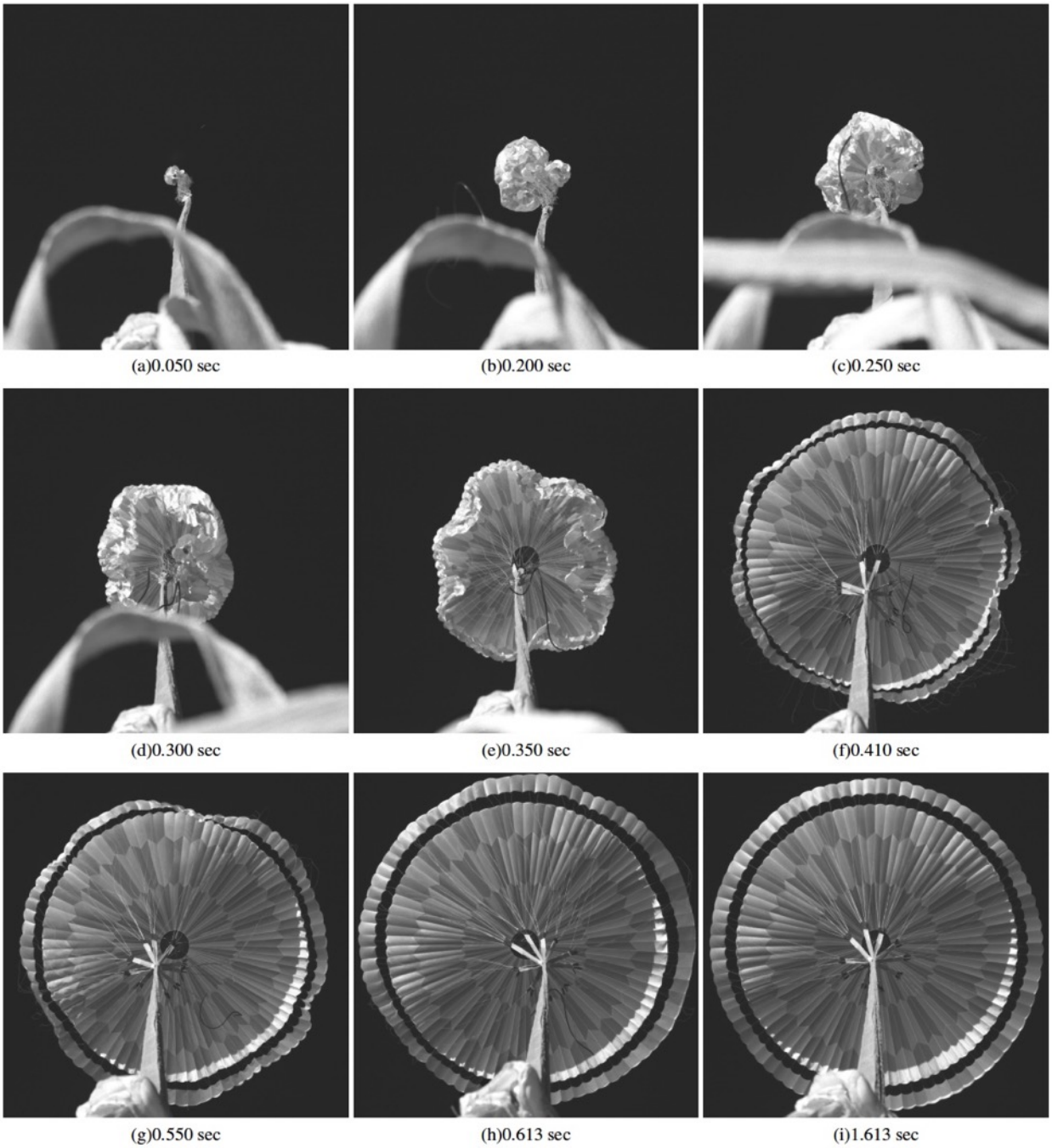

Figure 11 SR03 Parachute inflation sequence. Times show are relative to line stretch

Figure 11 shows a representative sequence of images of the inflating parachute, taken from one of the high speed cameras on the SR03 payload. The times indicated are from line-stretch: the instant when the parachute rigging has emerged from the pack and tension begins to develop on the parachute lines. Figure 12 shows the parachute aerodynamic forces as a function of time from line-stretch for the three ASPIRE flights. The aerodynamic forces generated by the parachutes were reconstructed using two separate methods: from the three load pins located at the parachute triple birdles, and from the accelerations measured by the IMU [18, 19]. In all the three flights, the parachute force increased rapidly and peak load was reached roughly half a second after line-stretch. This was followed by a

drop in force and a second peak whereafter the trace is near-monotonic. The peak force on the parachute increased from SR01 to SR02 to SR03. The magnitude of the post-peak decrease appears to exhibit the same trend.

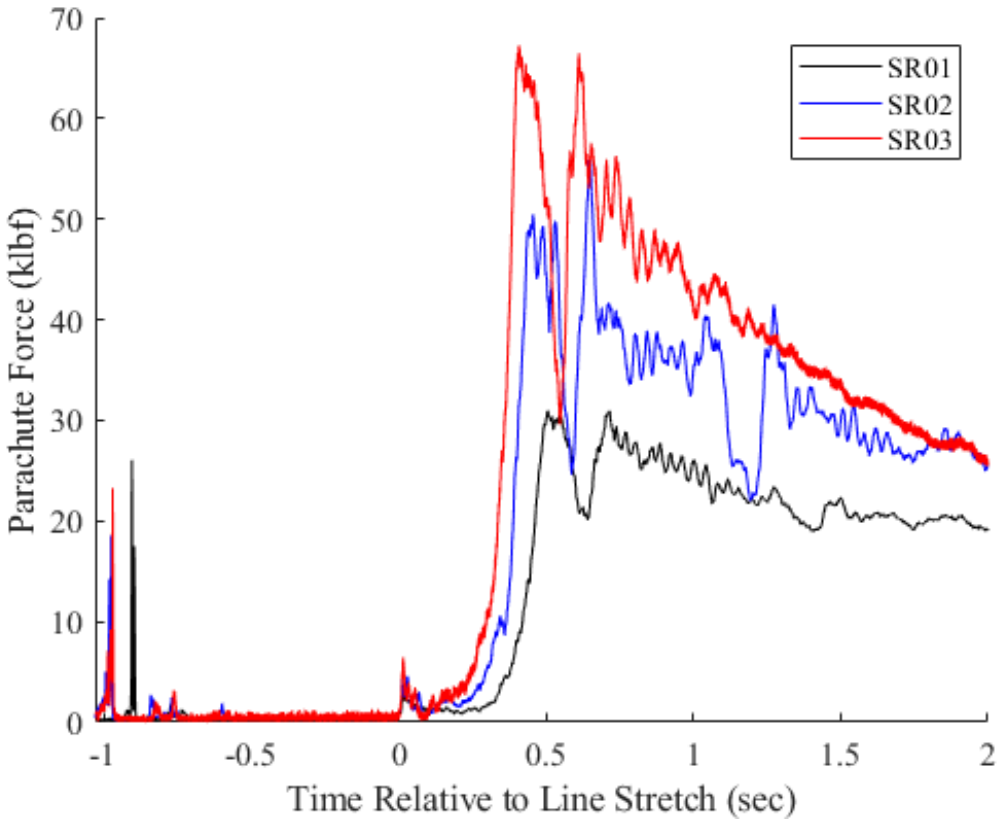

Figure 12 Reconstructed parachute aerodynamic force during the three ASPIRE flights, as measured by the load pins. Note that parachute forces are usually reported in klbf or kip; 1 klbf = 4.448 kN.

A. Inflation time

Following Greene [29], the time necessary for the DGB parachutes to achieve full inflation was predicted based on the time required for the payload to travel an inflation distance l_{inf}. This distance corresponds to the translation required for the parachute to ingest the volume of gas necessary to fully inflate the canopy and was modeled as:

$$\frac{l_{inf}}{D_0} = \alpha_{inf}\left(\frac{\rho_c}{\rho_\infty}\right)$$

Where ρ_c/ρ_∞ is the ratio of the stagnation density inside the canopy to the freestream density, assuming a normal shock develops ahead of the canopy. α_{inf} is a canopy-specific parameter related to the canopy geometry and effective inlet area during inflation. Based on prior tests of supersonic DGBs, α_{inf} was modeled as uniformly distributed from 3.75 and 5.5, with a nominal value of 4.5.

Table 4 Inflation time and non-dimensional inflation distance (α_{inf}) for the three ASPIRE flights

	Inflation time (sec)	α_{inf}
SR01	0.506	4.77
SR02	0.456	4.29
SR03	0.410	3.75
MSL	0.635	4.6

Table 44 shows the reconstructed values for the inflation time and α_{inf} for the three ASPIRE flights. The reconstructed values were found to be in excellent agreement with the pre-flight model, as well as with the performance observed during the MSL landing [30].

B. Inflation force

Table 5 shows the reconstructed parachute force at full inflation for the three flights, as well as the value of second peak in parachute force (Figure 12). The peak inflation force was predicted following the method outlined by Way [31]:

$$F_{peak} = k_p(2S_p q_\infty)$$

where the $(2S_p q_\infty)$ term represents the momentum flux entering a control volume around the inflating canopy (S_p is the projected area of the inflated canopy), and k_p is the fraction of the momentum flux which is converted to parachute drag. From analysis of prior DGB flights, Way proposed a uniform distribution of k_p between 0.7 and 0.9, with a nominal value of 0.8.

The reconstructed values of k_p for the first and second peaks in the three ASPIRE flights are listed in Table 5. The reconstructed peak inflation load and k_p from the MSL reconstruction are also included for reference. In general, the k_p values are in excellent agreement with pre-flight predictions. Note that during SR02, the second peak in load exceeded the first peak inflation load, resulting in a reconstructed $k_p = 0.93$. The occurrence of this large second peak in load is likely related to the force oscillations that are oftened observed in parachute deployments above Mach 1.4 and appear to be exacerbated at higher Mach numbers [30].

Table 5 Parachute inflation force and momentum transfer coefficient for the three ASPIRE flights

	1st peak force	k_p (1st peak)	2nd peak force	k_p (2nd peak)
SR01	32.4 klbf	0.77	32.3 klbf	0.79
SR02	50.9 klbf	0.78	55.8 klbf	0.93
SR03	67.4 klbf	0.76	66.5 klbf	0.84
MSL	35 klbf	0.83	-	-

C. Drag coefficient

Generation of the parachute drag model behind the (ASPIRE) slender body was made challenging by scarcity of pertinent data (featuring large Disk-Gap-Band parachutes, relevant trailing distance and Mach number, and a similar slender leading body). As a result, the pre-flight model was largely based on the MSL parachute drag model, with modifications to account for the differences in the leading body geometry, the latter being informed by both wind tunnel data and CFD simulations. References [32] and [33] present the details of existing data on DGB parachutes, and the sensitivity of parachute drag to the leading body geometry (slender body vs blunt body) and will not be repeated here.

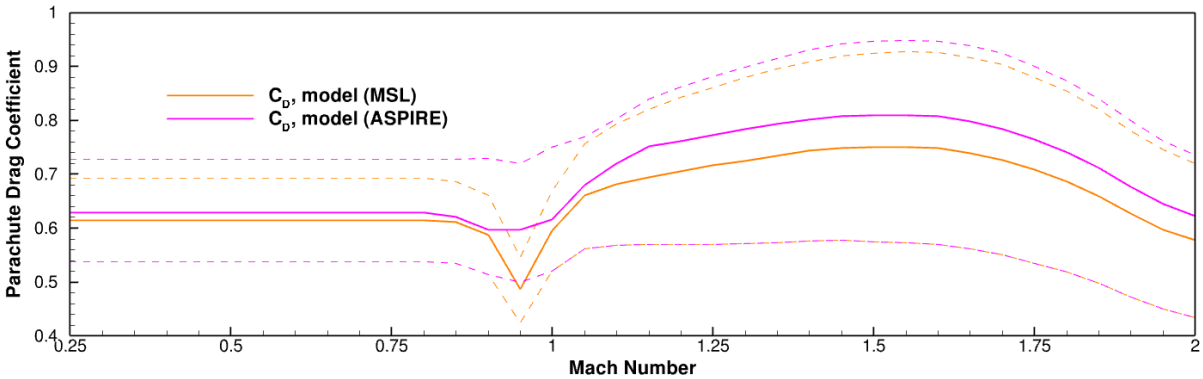

Figure 13 The pre-flight parachute drag model for ASPIRE along with that of MSL on which it is based. For both models, image shows the nominal drag curve (solid lines) and the upper and lower bounds (dashed lines).

Figure 13 shows the pre-flight parachute drag model along with the reference model for MSL and the uncertainty bounds of both. Note that the ASPIRE drag model features a smaller transonic decrease in drag and a higher nominal drag than the MSL drag model due to the differences in payload geometry. The ASPIRE forebody is roughly 1/6th the diameter of the MSL forebody, resulting a significantly smaller wake, reduction in the dynamic pressure deficit and a larger drag on the parachute.

The parachute drag force (F_D) was calculated for the three ASPIRE flights by projecting the reconstructed parachute force vector onto the wind-relative anti-velocity vector. The parachute drag coefficient was computed as:

$$C_D = \frac{F_D}{q_\infty S_0}$$

where S_0 is the parachute reference area. Figure 14(a) shows the reconstructed C_D as a function of Mach number for the three ASPIRE flights from 0.5 seconds after full inflation until splashdown (about 90 minutes of flight data), along with the pre-flight drag model. The total force coefficient from the MSL reconstruction is also included for reference [18]. Note that the flight data (ASPIRE and MSL) is a result of a rolling average of the force traces within bins of width Mach = 0.03. It is immediately apparent that the results from the three ASPIRE flights are in excellent agreement with each other across the range of Mach numbers where data is available. In addition, the flight results agree very closely with the pre-flight nominal C_D curve below Mach 0.75. However, above Mach 0.75, the flight results differ from the pre-flight model in two key ways.

First, there is no evidence of a sharp decline in the parachute C_D between Mach 0.8 and 1.1 (a transonic 'drag bucket') in the results for any of the flights. CFD simulations of rigid canopies in the wakes of slender and blunt bodies [15] suggest that the drag bucket observed in wind tunnel tests of parachutes deployed behind entry capsules [3, 19] may be the result of the expansion of the blunt body wake in the transonic regime and may thus not be applicable to the ASPIRE configuration.

Second, the reconstructed C_D profile between Mach 1.1 and 1.8 appears to be relatively flat and lower in magnitude than predicted by the pre-flight nominal model. Note that the reconstructed C_D agrees quite well with the MSL total force coefficient both below Mach 0.8 and above Mach 1. However, the transition from the near-constant supersonic C_D to the subsonic C_D appears to take place at lower Mach numbers in the ASPIRE tests. This may also be the result of the differences in the transonic behavior of blunt and slender body wakes [33].

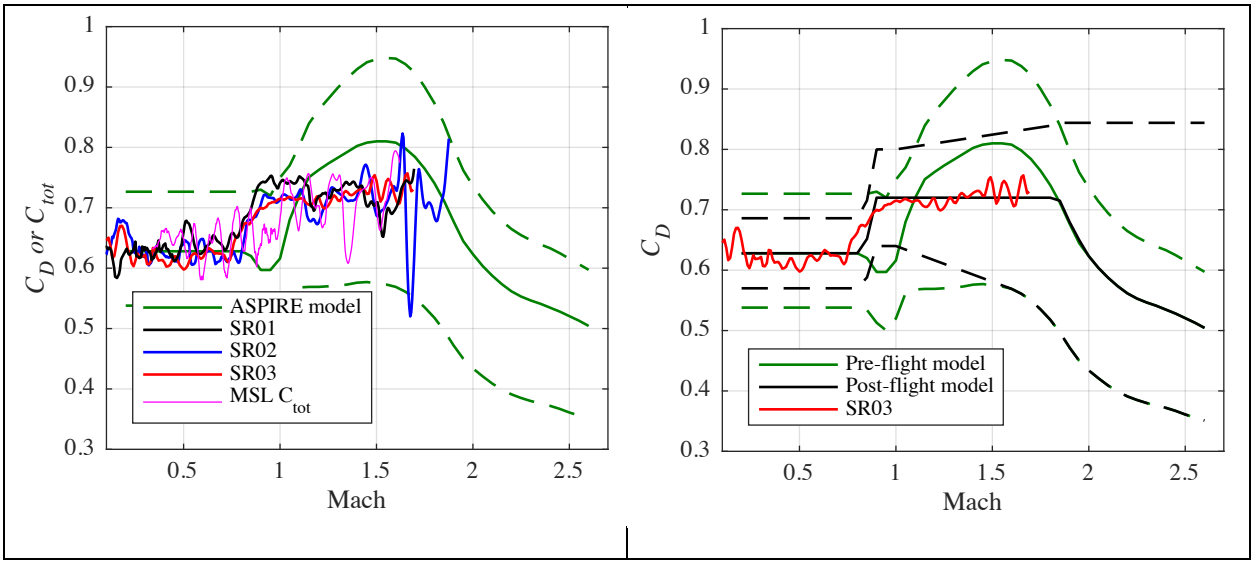

Figure 14(a) Comparison of reconstructed parachute drag coefficient (CD) with the pre-flight ASPIRE model and the reconstructed MSL total force coefficient. (b) Comparison of pre- and post-flight ASPIRE drag models.

Given these observations, following the three ASPIRE flight tests, an updated model for the C_D of DGBs deployed in the wake of a slender body was developed (Figure 14 b). At Mach numbers below 0.75, the nominal C_D curve is unchanged from the pre-flight model. Between Mach 0.75 and Mach 1.8, the nominal C_D curve is updated to provide better agreement with the average reconstructed C_D from the three ASPIRE flights. At Mach numbers above 1.8, there is very limited data for DGBs deployed behind slender bodies (a single flight test, and a single wind tunnel test, both featuring older parachute designs with shorter suspension lines [34,35]). In both the ASPIRE pre-flight and MSL models, the C_D was modeled as decreasing above Mach 1.6 based on wind tunnel results for DGBs tested behind a blunt body up to Mach 2.6 [36, 37]. Given the absence of new information above Mach 1.8, the nominal C_D curve was left unchanged from the pre-flight model above this Mach number.

Where appropriate, the upper and lower bounds on the ASPIRE drag model were updated to reflect the existence of new information. Below Mach 0.8, the upper and lower bounds were set at ±9.2% of the nominal curve. The updated bounds bracket the reconstructed C_D from the three ASPIRE flights. Above Mach 0.8, there is increased variability in

the reconstructed flight results. In addition, the volume of available data decreases with increased Mach number owing to the rapid deceleration of the ASPIRE system after parachute deploy. As a result, the upper and lower bounds increased linearly from ±9.2% of the nominal curve at Mach 0.8 to the pre-flight bounds at Mach 1.8. Above Mach 1.8, the upper bound in the updated model was fixed at $C_D = 0.844$ to account for the possibility that the drag coefficient of parachutes deployed behind slender bodies does not decrease between Mach 1.8 and 2.6.

The reasons for the discrepancy in the parachute's supersonic drag performance between the pre-flight model and flight tests is unclear. The pre-flight model relied on assumptions about the inflated shape of the canopy, the flow field at the location of the parachute in the wake of the slender payload, and the dynamics of the parachute and payload (payload and parachute angle of attack, etc). Stereoscopic reconstruction of the canopy shape and tracking of the canopy relative to the payload [38], and fluid-structure interaction (FSI) studies of inflating parachutes [39] are promising avenues for understanding the differences and for improving parachute models for future supersonic flights.

VI. Conclusions

NASA's ASPIRE project was launched to investigate the deployment and performance of supersonic Disk-Gap-Band parachutes at Mars-relevant conditions. A sounding rocket was utilized to deliver a slender body payload to high altitudes over Earth and deploy the parachutes at Mach numbers and dynamic pressures representative of a Mars descent. Flight Test Design requires aerodynamic models for the payload and for the parachute including peak aerodynamic force on the parachute and the parachute drag as a function of the Mach number.

Pre-flight aerodynamic models for the ASPIRE payload were based on Computational Fluid Dynamics (CFD) simulations of a smooth geometry at nominal and off-nominal conditions (Mach number, angle of attack) assuming a fully laminar and fully turbulent flow. Aerodynamic coefficients for this slender body have a significant viscous contribution resulting in differences between laminar and turbulent results. The aerodynamic models incorporated this feature by generating a nominal model as their average and ascertaining an uncertainty to cover the difference. Post-flight reconstruction and subsequent comparison of the model to the flight data indicates that (a) due to the low accelerations in regions of low dynamic pressure, the uncertainties in the measurement are of the magnitude of the measurements themselves, (b) there is a good agreement between the pre-flight models and the reconstructed aerodynamic behavior of the payload, and (c) the constructed payload is far from a smooth geometry and results in turbulent flow even at conditions where the flow over a smooth geometry payload should be laminar.

Generation of parachute models relied on existing MSL and Mars2020 models but were modified to account for the differences in payload geometry utilizing CFD simulations of the wakes of blunt and slender bodies and of a simplified rigid parachute behind each. All three ASPIRE flight tests resulted in a parachute inflations that were faster than that observed at Mars during Mars Science Laboratory, but within the range predicted by the pre-flight model. Similarly, the peak opening load on the parachute and the steady state aerodynamic drag on the parachute during the three flights were within the bounds of the pre-flight predictions. However, the pre-flight model over-predicted drag on the parachute during the first few seconds, during the supersonic portion of the flight. Finally, non-dimensionalized drag behavior across the three flights is remarkably similar, and exhibits little to no decrease in drag at transonic Mach numbers, as observed behind blunt bodies such as MSL and Mars2020 capsules.

Acknowledgments

This research was carried out at the Jet Propulsion Laboratory, California Institute of Technology, under a contract with the National Aeronautics and Space Administration. Suman Muppidi and John W. Van Norman are funded by NASA contracts NNA15BB15C and NNL12AA09C to AMA Inc., respectively.

References

[1] Cooley, C. G., and Lewis, J. G., "Viking 75 Project: Viking Lander System Primary Mission Performance Report," Tech. Rep. CR-145148, 1977.

[2] Galigher, L. L., "Aerodynamic Characteristics of Ballutes and Disk-Gap-Band Parachutes at Mach Numbers From 1.8 to 3.7," Tech. Rep. AEDC-TR-69-245, 1969.

[3] Bobbitt, P. J., Mayhue, R. J., Faurote, G. L., and Galigher, L. L., "Supersonic and SubsonicWind-Tunnel Tests of Reefed and Unreefed Disk-Gap-Band Parachutes," Tech. Rep. 1970-1172, 1970.

[4] Jaremenko, I., Steinberg, S., and Faye-Petersen, R., "Scale Model Test Results of the Viking Parachute System at Mach Numbers From 0.1 Through 2.6," Tech. Rep. CR-149377, 1971.

[5] Eckstrom, C. V., and Murrow, H. N., "Flight Tests of Cross, Modified Ringsail, and Disk-Gap- Band Parachutes from a Deployment Altitude of 3.05 km (10,000 ft)," Tech. Rep. TM X-2221, 1971.

[6] Eckstrom, C. V., and Preisser, J. S., " Flight Test of a 30-Foot-Nominal-Diameter Disk-Gap-Band Parachute Deployed at a Mach Number of 1.56 and a Dynamic Pressure of 11.4 Pounds Per Square Foot," Tech. Rep. TM X-1451, Aug 1967.
[7] J. S. Preisser and C. V. Eckstrom, "Flight Test of a 40-Foot-Nominal-Diameter Disk-Gap-Band Parachute Deployed at a Mach Number of 1.91 and a Dynamic Pressure of 11.6 Pounds Per Square Foot," Tech. Rep. TM X-1575, 1968.
[8] Preisser, J. S., and Grow, R. B., "High Altitude Flight Test of a Reefed 12.2-Meter Diameter Disk-Gap-Band Parachute With Deployment at a Mach Number of 2.58," Tech. Rep. TN D-6469, 1971.
[9] Moog, R. D., and Michel, F. D., "Balloon Launched Viking Decelerator Test Program Summary Report," Tech. Rep. CR-112288, 1973.
[10] E. J. Fallon, "System Design Overview of the Mars Pathfinder Parachute Decelerator Subsystem," AIAA Paper, no. 1997-1511, 1997.
[11] D. A. Spencer, R. Blanchard, R. D. Braun, P. H. Kallemeyn, and S. W. Thurman, "Mars Pathfinder Entry, Descent, and Landing Reconstruction," Journal of Spacecraft and Rockets , vol. 36, no. 3, pp. 357–365, May 1999.
[10] O'Farrell, C., Muppidi, S., Brock, J. M., Van Norman, J. W., and Clark, I. G., "Development of Models for Disk-Gap-Band Parachutes Deployed Supersonically in the Wake of a Slender Body", *2017 IEEE Aerospace Conference*, Big Sky, MT, 2017.
[11] Clark, I. G., and Tanner, C. L., "A Historical Summary of the Design, Development, and Analysis of the Disk-Gap-Band Parachute", *2017 IEEE Aerospace Conference*, Big Sky, MT, 2017.
[12] J. R. Cruz and J. S. Lingard, "Aerodynamic Decelerators for Planetary Exploration: Past, Present, and Future," AIAA Paper , no. 2006-6792, 2006.
[13] A. Witkowski and R. Bruno, "Mars Exploration Rover Parachute Decelerator System Program Overview," AIAA Paper , no. 2003-2100, 2003.
[14] D. S. Adams, A. Witkowski, and M. Kandis, "Phoenix Mars Scout Parachute Flight Behavior and Observations," IEEE Aerospace Conference Paper , no. 1534, 2011.
[15] J. R. Cruz, D. W. Way, J. D. Shidner, J. L. Davis, D. S. Adams, and D. S. Kipp, "Reconstruction of the Mars Science Laboratory Performance and Comparison to the Descent Simulation," AIAA Paper , no. 2013-1250, 2013.
[16] D. M. Kipp and D. Buecher, "A brief history of InSight parachute development and acceptance for flight," 15th International Planetary Probes Workshop , June 2018.
[17] C. L. Tanner, I. G. Clark, and A. Chen, "Overview of the Mars 2020 Parachute Risk Reduction Plan," IEEEAC Paper , 2018.
[18] O'Farrell, C., Karlgaard, C., Dutta, S., Queen, E., Ivanov, M., and Clark, I. G., "Overview and Reconstruction of the ASPIRE Project's SR01 Supersonic Parachute Test". *2018 IEEE Aerospace Conference*, Big Sky, MT, 2018
[19] O'Farrell, C., Sonneveldt, B. S., Karlgaard, C., Tynis, J. A., and Clark, I. G., "Overview of the ASPIRE Project's Supersonic Flight Tests of a Strengthened DGB Parachute", *2019 IEEE Aerospace Conference*, Big Sky, MT 2019
[20] Striepe, S.A., Powell, R.W., Desai, P.N., Queen, E.M., Way, D.W., Prince, J.L., Cianciolo, A.M., Davis, J.L., Litton, D.K., Maddock, R.M., Shidner, J.D., Winski, R.G., O'Keefe, S.A., Bowes, A.G., Aguirre, J.T., Garrison, C.A., Hoffman, J.A., Olds, A.D., Dutta, S., Zumwalt, C.H., White, J.P., Brauer, G.L., Marsh, S.M., "Program To Optimize Simulated Trajectories II (POST2): Utilization Manual," Vol. II, Version 3.0.NESC, 2014
[21] Balaram, J., Austin, R., Banerjee, P., Bentley, T., Henriquez, D., Martin, B., McMahon, E., and Sohl, G., "DSENDS - A High-Fidelity Dynamics and Spacecraft Simulator for Entry, Descent and Surface Landing," IEEE 2002 Aerospace Conference, Big Sky, Montana, March 9-16, 2002.
[22] Dutta, S., Queen, E. M., Bowes, A. L., Leylek, E.A., and Ivanov, M., "ASPIRE Flight Mechanics Modeling and Post Flight Analysis", AIAA Aviation Forum, Atlanta, GA, June 2018.
[23] Sonneveldt, B., Clark, I. G., and O'Farrell, C, "Summary of the Advanced Supersonic Parachute Inflation Research Experiment (ASPIRE) Sounding Rocket Tests with a Disk-Gap-Band Parachute", AIAA Aviation Forum, Dallas, TX, 2019.
[24] Nichols, R.H., and Buning, P.G., "User's Manual for OVERFLOW 2.2," Version 2.2, August 2010.
[25] FUN3D, "Fully Unstructured Navier-Stokes", Available: fun3d.larc.nasa.gov.
[26] Wright, M. J., White, T. R., and Mangini, N., "Data Parallel Line Relaxation (DPLR) Code User Manual: Acadia – Version 4.01.1", Tech. Rep., NASA TM 2009-215388, 2009.
[27] Karlgaard, C.D., Tynis, J., and O'Farrell, C., "Reconstruction of the Advanced Supersonic Parachute Inflation Research Experiment Sounding Rocket Flight Test", AIAA Aviation Forum, Atlanta, GA, June 2018.
[28] Karlgaard, C.D., Tynis, J., Sonneveldt, B., and O'Farrell, C., "Reconstruction of the Advanced Supersonic Parachute Inflation Research Experiment Sounding Rocket Flight Tests with Strengthened Dist-Gap-Band Parachute", AIAA Scitech Forum, San Diego, CA, Jan 2019.
[29] Greene, G. C., "Opening Distance of a Parachute," *Journal of Spacecraft and Rockets*, vol. 7, no. 1, 1970.
[30] Cruz, J. R., Way, D. W., Shidner, J. D., Davis, J. L., Powell, R. W., Kipp, D. M., Adams, D. S., Witkowski, A., and Kandis, M., "Reconstruction of the Mars Science Laboratory Performance and Comparison to the Descent Simulation," AIAA Paper 2013-1276, 2013.

[31] Way, D. W., "A Momentum-Based Method for Predicting the Peak Opening Load for Supersonic Parachutes". *2018 IEEE Aerospace Conference*, Big Sky, MT, 2018
[32] O'Farrell, C., Muppidi, S., Brock, J. M., Van Norman, J. W., and Clark, I. G., "Development of Models for Disk-Gap-Band Parachutes Deployed Supersonically in theWake of a Slender Body", *2017 IEEE Aerospace Conference*, Big Sky, MT, 2017.
[33] Muppidi, S., O'Farrell, C., Tanner, C. L., and Clark, I. G., "Modeling and Flight Performance of Supersonic Disk-Gap-Band Parachutes in Slender Body Wakes", *2018 Atmospheric Flight Mechanics Conferences, AIAA AVIATION Forum*, Atlanta, GA, (AIAA 2018-3623), 2018.
[34] Eckstrom, C. V., and Preisser, J. S., Flight Test of a 40-Foot-Nominal-Diameter Disk-Gap-Band Parachute Deployed at a Mach Number of 2.72 and a Dynamic Pressure of 9.72 Pounds per Square Foot," Tech. Rep. TM X-1623, Aug 1968.
[35] Galigher, L. L., "Aerodynamic Characteristics of Ballutes and Disk-Gap-Band Parachutes at Mach Numbers From 1.8 to 3.7" AEDC Technical Report AEDC-TR-69-245, 1969.
[36] Reichneau, D. E. A., "Aerodynamic Characteristics of Disk-Gap-Band Parachutes in the Wake of Viking Entry Forebodies at Mach Numbers From 0.2 to 2.6," AEDC Technical Report AEDC-TR-72-78, 1972.
[37] Sengupta, A., Roeder, J., Kelsch, R., Wernet, M., Kandis, M., and Witkowski, A., "Supersonic Disk Gap Band Parachute Performance in the Wake of a Viking-Type Entry Vehicle from Mach 2 to 2.5," *AIAA Paper* 2008-6217, 2008.
[38] Rabinovitch,J, Griffin, G., Seto, W., O'Farrell, C. , Tanner, C., and Clark, I., "ASPIRE Supersonic Parachute Shape Reconstruction: Experimental Results and Comparisons to Simulations," *AIAA Paper*, no. 2009-1629, 2019.
[39] Placeholder, Rabinovitch,J, et al AIAA Avitation Paper TBD 2019